Synthesis of Tellurium Dioxide Nanoparticles by Spray Pyrolysis

Hongwang Zhang and Mark T. Swihart*

Department of Chemical and Biological Engineering, University at Buffalo, The State University of New York, Buffalo, New York, 14260-4200

Received September 20, 2006

Tellurite glasses (amorphous TeO_2 based materials) have two useful optical properties, a high refractive index and high optical nonlinearity, that make them attractive for a range of applications. Unlike other metal oxide nanoparticles that are prepared in large quantities by vapor-phase processes, TeO_2 nanoparticles have not been prepared by such methods. Here, we describe the vapor-phase synthesis of TeO_2 nanoparticles from an aqueous solution of telluric acid, $Te(OH)_6$, that is dispersed into fine droplets by an atomizer. These droplets are carried by nitrogen through a furnace, where they evaporate and decompose, resulting in nucleation of TeO_2 nanoparticles. The resulting nanoparticles were characterized by TEM, XPS, FTIR, and XRD. Particle size distributions measured online using a scanning mobility particle spectrometer demonstrated that a furnace temperature above 700 °C was required for full evaporation of the precursor droplets. Thermogravimetric analysis shows that the $Te(OH)_6$ converts to TeO_2 without evaporating when heated at 5−100 °C/min. This contrasts sharply with the complete evaporation observed in the spray pyrolysis reactor, where heating rates exceed 50 000 °C/min. The effects of operating parameters on nanoparticle composition, production rate, and size were also studied. This laboratory scale process is capable of producing up to 80 mg/h amorphous TeO_2 nanoparticles with primary particle diameters from 10 to 40 nm. Particles this small exhibit negligible scattering of visible light and have potential applications in the linear and nonlinear refractive index engineering of polymer nanocomposites and as host matrices for rare-earth ions that can act as IR to visible upconverters. The method presented here allows their synthesis in macroscopic quantities from an inexpensive and environmentally friendly precursor.

Introduction

Tellurite glasses (amorphous TeO_2 or telluria, usually doped with other materials) have been a subject of research for many years because of their useful optical properties: a high refractive index ($n = 2-2.25$) and high optical nonlinearity ($\chi^{(3)} = 10^{-13}$ to 4×10^{-12} esu).[1,2] For comparison, SiO_2 has $n \approx 1.5$ and $\chi^{(3)} \approx 3 \times 10^{-14}$ esu. These optical properties of tellurite glasses make them attractive for a range of applications from high-index optical elements to second- and third-harmonic generation. While bulk tellurite glasses have been widely studied during the past 50 years, there has been relatively little work on the formation of telluria and tellurite glasses as fine particles or nanoparticles. Nanoparticles of other metal oxides (silica, titania, etc.) find a wide array of uses. Tellurium dioxide based nanoparticles would be particularly interesting for the formation of polymer/nanoparticle nanocomposites with a high refractive index and high optical nonlinearity. Because of the high refractive index of TeO_2, particles of it are very efficient scatterers of light. Nevertheless, if the particles are made small enough, roughly less than 1/10th of the wavelength of light, they will no longer be efficient scatterers. Thus, particles smaller than 30−50 nm in diameter can potentially be dispersed in a transparent polymer matrix to produce a transparent nanocomposite with a refractive index and optical nonlinearity much higher than could be obtained in the polymer alone. Use of photopatternable polymers, like PMMA or other acrylates, could allow lithographic writing of high-index microscale optical elements from these nanocomposites.

The conventional means of producing tellurite glasses is the melting and quenching technique. However, it is difficult to obtain pure (undoped) TeO_2 glasses by this method. The addition of various other oxides is usually required to prevent crystallization. Another method for preparing tellurite glasses is the sol−gel process, which has been presented in several studies.[3−8] However, this method has only been used for preparing tellurite glass films, and there may be difficulties in scaling it to higher production rates or the production of bulk quantities of TeO_2. As compared to other metal-oxide nanoparticles, particularly silica, titania, and zinc oxide, which are well-studied[9−14] and prepared commercially in large quantities by vapor-phase processes, the production of

* Corresponding author. Tel.: (716) 645-2911 (ext 2205). Fax: (716) 645-3822. E-mail: swihart@eng.buffalo.edu.

(1) Vogel, E. M.; Weber, M. J.; Krol, D. M. *Phys. Chem. Glasses* **1991**, *32*, 231.
(2) El-Mallawany, R. A. H. *Tellurite Glasses Handbook: Physical Properties and Data*; CRC Press: Boca Raton, FL, 2002.
(3) Coste, S.; Lecomte, A.; Thomas, P.; Champarnaud-Mesjard, J. C.; Merle-Mejean, T.; Guinebretiere, R. *J. Non-Cryst. Solids* **2004**, *345−346*, 634.
(4) Hodgson, S. N. B.; Weng, L. *J. Non-Cryst. Solids* **2000**, *276*, 195.
(5) Hodgson, S. N. B.; Weng, L. *J. Sol-Gel Sci. Technol.* **2000**, *18*, 145.
(6) Weng, L.; Hodgson, S. N. B. *Opt. Mater.* **2002**, *19*, 313.
(7) Weng, L.; Hodgson, S.; Bao, X.; Sagoe-Crentsil, K. *Mater. Sci. Eng., B* **2004**, *107*, 89.
(8) Pierre, A.; Duboudin, F.; Tanguy, B.; Portier, J. *J. Non-Cryst. Solids* **1992**, *147*, 569.
(9) Xia, B.; Lenggoro, I. W.; Okuyama, K. *Adv. Mater.* **2001**, *13*, 1579.
(10) Xia, B.; Lenggoro, I. W.; Okuyama, K. *Chem. Mater.* **2002**, *14*, 2623.

10.1021/cm062257n CCC: $37.00
Published on Web 02/23/2007

telluria by these methods does not appear to have been previously studied.

In recent years, several groups have made important advances in the synthesis of nanoparticles by spray pyrolysis and demonstrated its versatility in producing particles of a variety of compositions, shapes, and sizes. A few representative examples are provided here to put the present work in perspective. Laine's group used liquid-feed flame spray pyrolysis (LF-FSP) to produce mixed metal oxide nanopowders containing aluminum with a variety of other metals (Ni, Co, Y, and others),[15−19] with potential applications in high-quality aluminum ceramics and nanocomposites. Pratsinis's group developed a flame spray pyrolysis (FSP) process to synthesize a series of metal/metal oxides at high production rates, which could be used for catalysts, sensors, and biomaterials.[20−28] They also made shape controlled ZnO nanorods by FSP recently.[29] Okuyama's group has prepared many different nano- and microparticles by spray pyrolysis[12,30−32] and has developed the salt assisted spray pyrolysis (SAD) method to prevent agglomeration of multiple particles formed within a single aerosol droplet.[9,10,33] Suslick and Didenko have used ultrasonic spray pyrolysis (USP) to produce semiconductor nanocrystals within aerosol droplets[34] and to produce microparticles with an internal nanostructure.[35,36] Likewise, Brinker and co-workers have produced microparticles with an internal periodic nanostructure using the evaporation assisted self-assembly process.[37−39] In most of the previous work, microparticles, often with an internal nanoscale structure, have been formed by reactions within precursor droplets that do not fully evaporate, while much smaller nanoparticles are formed in methods such as flame spray pyrolysis, where precursor droplets evaporate fully and particles nucleate from the vapor phase.

The synthesis of tellurium dioxide nanoparticles by a spray pyrolysis method is described in this paper. In this method, nanoparticles are prepared in the gas phase, starting from solution-phase precursors. A solution of the nanoparticle precursor compound(s) is sprayed as fine droplets (ranging from <0.1 to >3 μm in diameter) that evaporate partially or totally, depending on the volatility of the solvent and precursor. In the present case, precursor droplets evaporate completely for most operating conditions. The precursors are converted into nanoparticles thermally in a high-temperature furnace. The effects of operating parameters on nanoparticle composition, production rate, and average size were studied. In addition to chemical and structural analysis of the collected particles, a scanning mobility particle spectrometer (SMPS) system was used to make online measurements of the size distribution of the nanoparticles. This provided a clear demonstration that the particle formation occurs via complete evaporation of the precursor droplets followed by nucleation of product particles. It also showed that the evaporation dynamics for these small particles at high heating rates are dramatically different from those of bulk $Te(OH)_6$ at lower heating rates.

Experimental Procedures

The reactor system used in the experiments described here is shown schematically in Figure 1. A key component of this reactor system is the atomizer (Collison type, BGI, Waltham, MA, three-jet model) that converts a liquid precursor solution into small aerosol droplets that are carried by nitrogen (99.8%) into the reactor. This atomizer produces droplets with a broad size distribution, ranging from <100 nm to >3 μm, with a count median diameter of about 0.2 μm and a mass median diameter of about 2.0 μm. For making telluria nanoparticles, we used a solution of telluric acid ($Te(OH)_6$, 99 wt %, Aldrich) in deionized water (Millipore, 18 mΩ) as the precursor. The concentration of telluric acid in the precursor solution ranged from 10 to 100 g/L. Large droplets were removed from the precursor stream by a mist arrestor (a line filter housing typically used for compressed air filtration, with the filter element removed, MSC Direct part 60032000). Water vapor was removed from the precursor aerosol by a home-built diffusion drier to prevent recondensation of water on the final product powder. Air (standard grade) was added to ensure that excess oxygen was present and that tellurium oxide, rather than metallic tellurium, would be produced. The precursor aerosol then flowed through a 1 in. diameter Inconel tube heated by a three-zone electric furnace with a total heated length of 76 cm, which provided the high temperature (600−1000 °C) needed to convert the telluric acid to tellurium oxide

(11) Mueller, R.; Madler, L.; Pratsinis, S. E. *Chem. Eng. Sci.* **2003**, *58*, 1969.
(12) Okuyama, K.; Lenggoro, I. W. *Chem. Eng. Sci.* **2003**, *58*, 537.
(13) Seo, D. J.; Park, S. B.; Kang, Y. C.; Choy, K. L. *J. Nanoparticle Res.* **2003**, *5*, 199.
(14) Kim, S. H.; Liu, B. Y. H.; Zachariah, M. R. *Chem. Mater.* **2002**, *14*, 2889.
(15) Azurdia, J.; Marchal, J.; Laine, R. M. *J. Am. Ceram. Soc.* **2006**, *89*, 2749.
(16) Azurdia, J. A.; Marchal, J.; Shea, P.; Sun, H. P.; Pan, X. Q.; Laine, R. M. *Chem. Mater.* **2006**, *18*, 731.
(17) Laine, R. M.; Marchal, J.; Sun, H. P.; Pan, X. Q. *Adv. Mater.* **2005**, *17*, 830.
(18) Kim, S.; Gislason, J. J.; Morton, R. W.; Pan, X. Q.; Sun, H. P.; Laine, R. M. *Chem. Mater.* **2004**, *16*, 2336.
(19) Baranwal, R.; Villar, M. P.; Garcia, R.; Laine, R. M. *J. Am. Ceram. Soc.* **2001**, *84*, 951.
(20) Strobel, R.; Madler, L.; Piacentini, M.; Maciejewski, M.; Baiker, A.; Pratsinis, S. E. *Chem. Mater.* **2006**, *18*, 2532.
(21) Stark, W. J.; Grunwaldt, J. D.; Maciejewski, M.; Pratsinis, S. E.; Baiker, A. *Chem. Mater.* **2005**, *17*, 3352.
(22) Loher, S.; Stark, W. J.; Maciejewski, M.; Baiker, A.; Pratsinis, S. E.; Reichardt, D.; Maspero, F.; Krumeich, F.; Gunther, D. *Chem. Mater.* **2005**, *17*, 36.
(23) Strobel, R.; Pratsinis, S. E.; Baiker, A. *J. Mater. Chem.* **2005**, *15*, 605.
(24) Jossen, R.; Pratsinis, S. E.; Stark, W. J.; Madler, L. *J. Am. Ceram. Soc.* **2005**, *88*, 1388.
(25) Mueller, R.; Jossen, R.; Pratsinis, S. E.; Watson, M.; Akhtar, M. K. *J. Am. Ceram. Soc.* **2004**, *87*, 197.
(26) Sahm, T.; Madler, L.; Gurlo, A.; Barsan, N.; Pratsinis, S. E.; Weimar, U. *Sens. Actuators, B* **2004**, *98*, 148.
(27) Jossen, R.; Mueller, R.; Pratsinis, S. E.; Watson, M.; Akhtar, M. K. *Nanotechnology* **2005**, *16*, 609.
(28) Beaucage, G.; Kammler, H. K.; Mueller, R.; Strobel, R.; Agashe, N.; Pratsinis, S. E.; Narayanan, T. *Nat. Mater.* **2004**, *3*, 370.
(29) Height, M. J.; Madler, L.; Pratsinis, S. E.; Krumeich, F. *Chem. Mater.* **2006**, *18*, 572.
(30) Xia, B.; Lenggoro, I. W.; Okuyama, K. *Chem. Mater.* **2002**, *14*, 4969.
(31) Lenggoro, I. W.; Xia, B.; Mizushima, H.; Okuyama, K.; Kijima, N. *Mater. Lett.* **2001**, *50*, 92.
(32) Chang, H. W.; Lenggoro, I. W.; Ogi, T.; Okuyama, K. *Mater. Lett.* **2005**, *59*, 1183.
(33) Xia, B.; Lenggoro, I. W.; Okuyama, K. *J. Mater. Chem.* **2001**, *11*, 2925.
(34) Didenko, Y. T.; Suslick, K. S. *J. Am. Chem. Soc.* **2005**, *127*, 12196.
(35) Suh, W. H.; Jang, A. R.; Suh, Y. H.; Suslick, K. S. *Adv. Mater.* **2006**, *18*, 1832.
(36) Suh, W. H.; Suslick, K. S. *J. Am. Chem. Soc.* **2005**, *127*, 12007.
(37) Jiang, X. M.; Brinker, C. J. *J. Am. Chem. Soc.* **2006**, *128*, 4512.
(38) Brinker, C. J.; Lu, Y. F.; Sellinger, A.; Fan, H. Y. *Adv. Mater.* **1999**, *11*, 579.
(39) Lu, Y. F.; Fan, H. Y.; Stump, A.; Ward, T. L.; Rieker, T.; Brinker, C. J. *Nature* **1999**, *398*, 223.

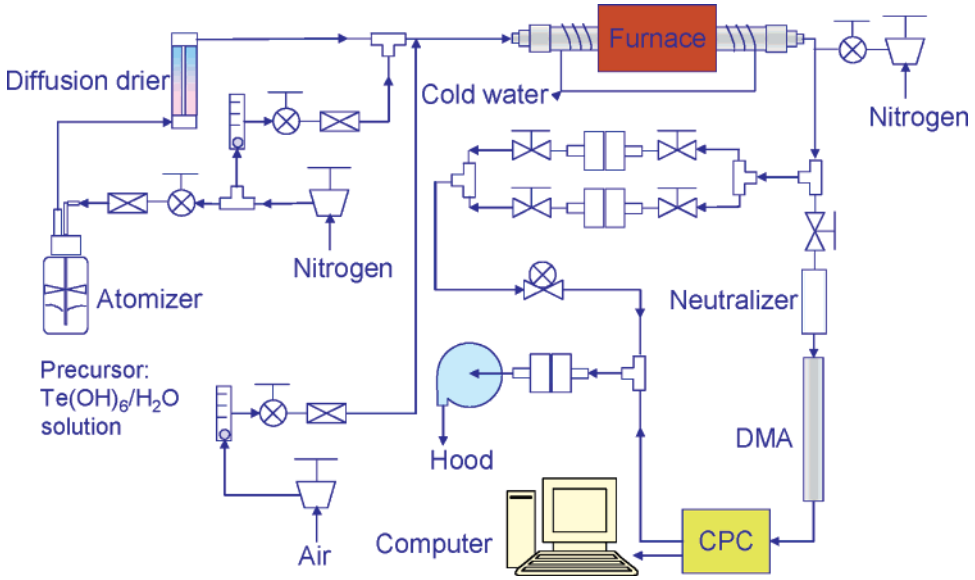

Figure 1. Schematic drawing of the reactor system for the synthesis of tellurium dioxide nanoparticles by spray pyrolysis.

nanoparticles. The residence time within the reactor was approximately 0.5 s under typical operating conditions. The resulting nanoparticles were collected on polyvinylidene fluoride (PVDF) membrane filters (Millipore) with a 0.22 μm nominal pore size.

Surface elemental analysis of the nanoparticles by X-ray photoelectron spectroscopy (XPS) was performed on a Physical Electronics/PHI 5300 X-ray photoelectron spectrometer. The particle size and morphology were characterized by transmission electron microscopy (TEM) using a JEOL JEM 2010 microscope at an acceleration voltage of 200 kV or using a JEOL JEM 100CX microscope at an acceleration voltage of 80 kV. To prepare TEM grids for imaging, powder samples that had been collected on PVDF membrane filters were dispersed into methanol at a low concentration, typically ~1 μg/mL. Several drops of this dispersion were dropped onto a carbon-coated TEM grid, and the solvent was allowed to evaporate in air. For crystalline nanoparticles, selected area electron diffraction was performed in the TEM. The specific surface area of the particles was measured by nitrogen physisorption (the BET method, Micromeretics Model 2010 ASAP Physisorption Apparatus), and the average primary particle size was estimated based on the measured specific surface area by assuming that the primary particles were spherical. For crystalline nanoparticles, wide-angle powder X-ray diffraction (XRD, Siemens D500) was used to characterize powder samples and to identify the crystalline phases present.

The size distribution of the nanoparticles was monitored by a scanning mobility particle spectrometer (SMPS) system. The home-built SMPS system included a ^{210}Po bipolar charger (neutralizer), a differential mobility analyzer (DMA model 3081, TSI Instruments, Shoreview, MN), a condensation particle counter (CPC model 3010, TSI Instruments, Shoreview, MN), and appropriate flow and voltage controllers, interfaced to a PC and controlled using LabView. In this system, the nanoparticles first pass through the bipolar neutralizer, which establishes an equilibrium (Boltzmann) charge distribution among them, so that a known fraction of particles of a given size are charged. In the DMA, which has an inner cylinder connecting to a power supply (0 to −10 000 VDC), the charged nanoparticles are separated according to their electrical mobility. The separated nanoparticles are counted by the CPC. The resulting particle count versus DMA voltage data was inverted to obtain the distribution of particle concentration versus particle size using our own data inversion program that accounts for multiply charged particles and particle diffusion within the DMA, as previously described.[40] The particles were diluted with nitrogen at the reactor exit, to reduce the total particle concentration to a level that could be reliably measured by the SMPS, and to reduce aggregation in the sampling line leading to the SMPS. The dilution factor is not precisely known but remained constant within a given set of experiments.

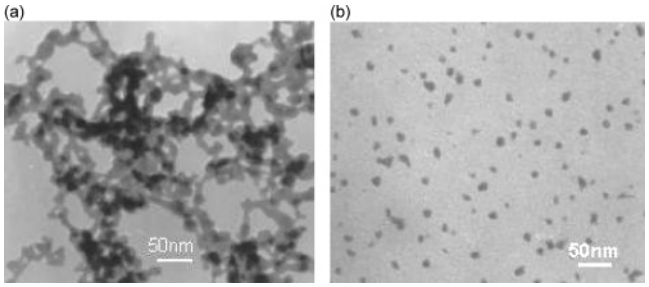

Figure 2. TEM images of (a) agglomerated telluria nanoparticles dropcast from a ~1 mg/mL dispersion and (b) well-dispersed telluria nanoparticles dropcast from a ~1 μg/mL dispersion. In both cases, particles were dispersed in methanol at room temperature, using mild sonication that did not result in significant sample heating.

Results and Discussion

Basic Morphology and Properties of Tellurium Dioxide Nanoparticles. The as-produced telluria nanoparticles were amorphous and white. TEM images of the amorphous TeO_2 particles are shown in Figure 2. The particles are somewhat polydisperse in size, with the primary particle diameter ranging from 10 to 20 nm. The telluria nanoparticles did not disperse well in most solvents. Clear dispersions in semipolar solvents such as methanol could be obtained only at extremely low concentrations (micrograms per milliliter). Dispersions prepared at higher concentrations appeared cloudy, and particles sedimented out of these dispersions on a time scale of a few hours. TEM images of particles dropcast from these relatively high concentration dispersions (milligrams per milliliter) showed large agglomerates, as seen in Figure 2a. However, TEM images of particles dropcast from very dilute dispersions (~1 μg/mL) showed well-

(40) Talukdar, S. S.; Swihart, M. T. *Aerosol Sci. Technol.* **2003**, *37*, 145.

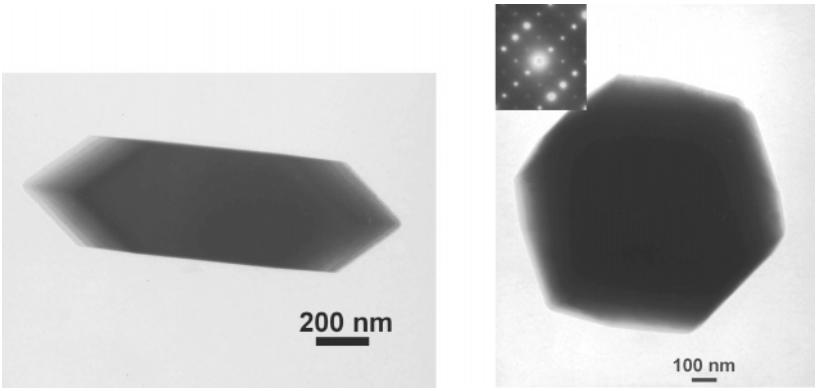

Figure 3. Tellurium dioxide microcrystals formed upon dispersion of amorphous TeO_2 nanoparticles in water. The inset is the selected area electron diffraction pattern from the microcrystal shown.

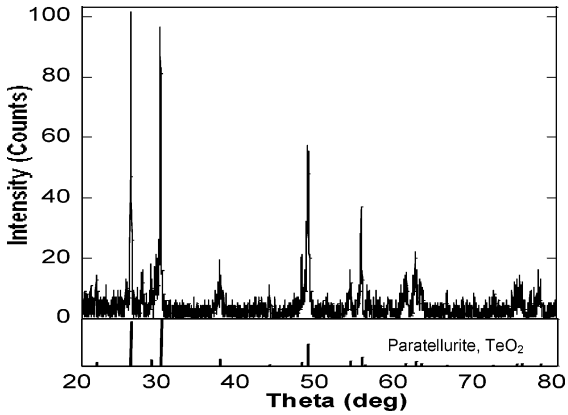

Figure 4. XRD spectrum from paratellurite particles formed when amorphous telluria nanoparticles were dispersed in deionized water.

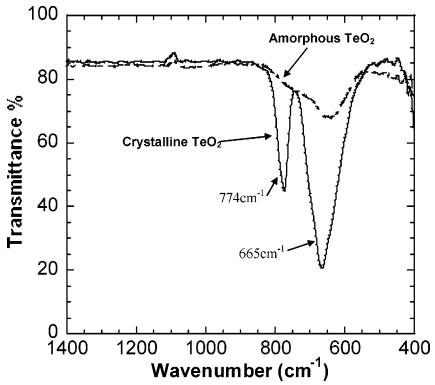

Figure 5. FTIR spectra from amorphous and crystalline TeO_2 particles.

dispersed primary particles, as seen in Figure 2b. The image in Figure 2a is similar in appearance to hard agglomerates sometimes formed in vapor-phase material synthesis processes. However, the fact that isolated nanoparticles are observed when the particles are dispersed at sufficiently low concentrations demonstrates that hard agglomerates are not formed during the vapor-phase synthesis.

When the particles were dispersed in water at neutral or acidic pH at room temperature, they did not remain as amorphous nanoparticles; instead, they grew into much larger crystals. These were single crystals with dimensions on the order of a micrometer, as shown in Figure 3. This suggests that the amorphous TeO_2 particles are somewhat soluble in water at neutral or acidic pH and that they can therefore undergo an Ostwald ripening process in which material is transferred from less stable small, amorphous particles to more stable large crystalline particles. X-ray diffraction (XRD) and infrared (FTIR) spectroscopy provided limited information on the amorphous nanoparticles. However, for the crystallized nanoparticles, these methods gave a clear demonstration that the paratellurite phase of TeO_2 had formed. The XRD spectrum of these crystals is shown in Figure 4. The lines below the experimental spectrum show the peak positions and relative intensities for paratellurite. Comparison with reference spectra showed that the crystals formed in water were paratellurite, which has a tetragonal crystal structure, and were not the orthorhombic phase of TeO_2. The FTIR spectra for both amorphous and crystallized particles are shown in Figure 5. The upper spectrum is for the amorphous nanoparticles. It exhibits a single broad peak between 600 and 800 cm^{-1}. The lower spectrum is for the crystals formed after dispersing the amorphous particles in water. It exhibits two peaks, at 665 and at 774 cm^{-1}. The peak at 774 cm^{-1} is characteristic of paratellurite.[2,7] This provides further conformation that the as-produced particles are amorphous telluria and that the crystals formed in water are paratellurite. The strong peak around 665 cm^{-1} arises from the Te−O bond in a $[TeO_4]$ unit with a trigonal bipyramidal structure.[7]

Parametric Study of the Effect of Operating Conditions on Particle Size and Properties. Many experimental parameters such as furnace temperature, precursor concentration, pressure supplied to the atomizer, total system pressure, and gas flow rates can affect the nanoparticle production rate, size, and morphology. The most important effects are described next.

Effect of Furnace Temperature. Furnace temperature affected the composition of the TeO_2 particles produced. If the temperature was too low, the precursor did not fully decompose. For very high temperatures, there was an increased possibility of incorporation of metals from the reactor tube as well as the production of metallic tellurium rather than fully oxidized TeO_2. For all of the results described here, the three heating zones of the furnace were all kept at the same temperature, which was 600, 800, or 1000 °C. The nanoparticles were examined by X-ray photoelectron spectroscopy (XPS), which showed only peaks for Te and O, plus a small carbon peak from atmospheric contamination. An XPS survey spectrum from particles produced at 800 °C is shown in Figure 6. The nanoparticles

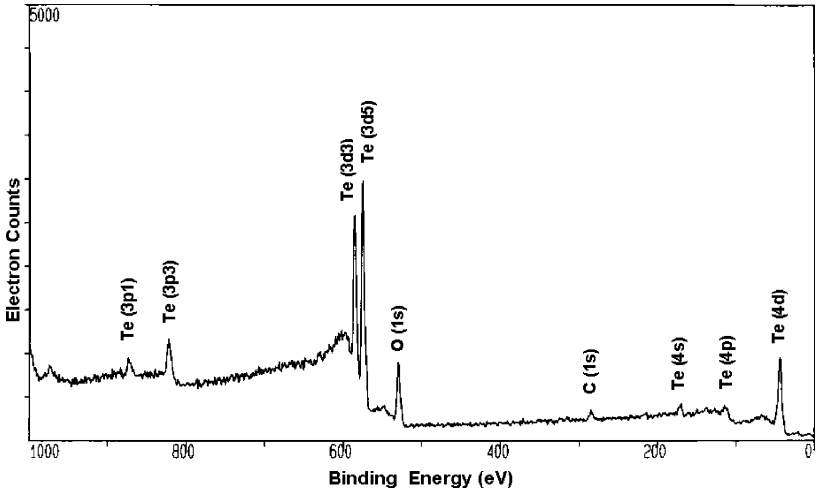

Figure 6. XPS survey spectrum for telluria nanoparticles produced at 800 °C.

Table 1. Typical Reaction Parameters

precursor concentration	operating pressure	furnace temperature	pressure supplied to atomizer	air flow rate	added nitrogen flow rate
50 g/L	14 psia	800 °C	40 psi	2 L/min	0 L/min

produced at 600 °C were slightly yellow. XPS measurements showed O_{1s} and $Te_{3d5/2}$ peaks at binding energies of 531.9 and 577.7 eV, from which we conclude that the particles contained $Te(OH)_6$ (Te in its +6 oxidation state). That is, they consisted primarily of unreacted precursor. The nanoparticles produced at 800 °C were white. The O_{1s} and $Te_{3d5/2}$ peaks in the XPS spectrum were at binding energies of 530.7 and 575.8 eV, which are consistent with tellurium dioxide (Te in its +4 oxidation state). The nanoparticles produced at 1000 °C were usually also white. In a few experiments, they appeared somewhat silver, indicating the possible presence of metallic tellurium. In a few other experiments, the particles appeared slightly yellow. Because operation at 800 °C consistently yielded stoichiometric TeO_2, this temperature was used in all subsequent experiments described here.

Effect of Precursor Concentration. The precursor concentration has important effects on the particle size and production rate. A series of precursor solutions with $Te(OH)_6$ concentrations of 10, 30, 50, 70, and 100 g/L were used. The production rate was calculated by weighing the telluria nanoparticles collected on filter paper downstream of the reactor and dividing by the reaction time. We estimated the average nanoparticle size from measurements of specific surface area, assuming the nanoparticles were spheres with the density of bulk paratellurite. This method gives the surface area mean diameter, also known as the Sauter mean diameter. For a polydisperse sample, this is larger than the number mean diameter. In this series of experiments, we fixed all other operating conditions at the values shown in Table 1 and only changed the precursor concentration. The production rates and surface area mean diameters are shown in Figure 7.

Both the nanoparticle production rate and the average particle size increased monotonically with increasing precursor concentration. The gas flow rate through the atomizer

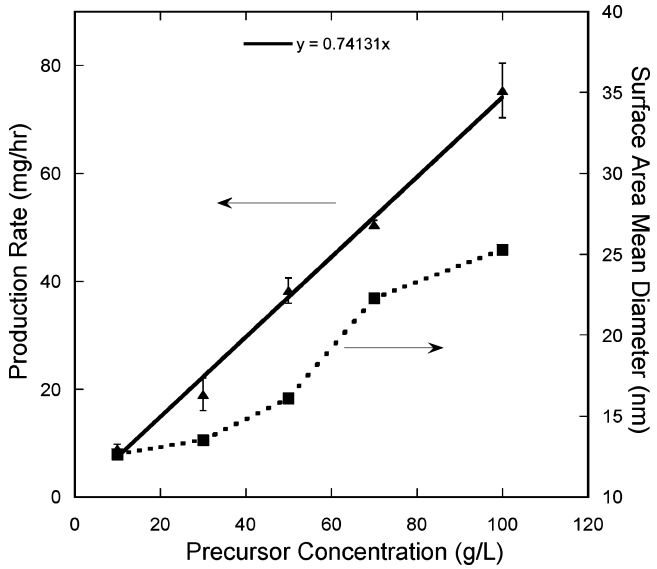

Figure 7. Effect of precursor concentration on the TeO_2 nanoparticle production rate and surface area mean diameter. Error bars on the production rate are one standard deviation based on three to five replicates. The line through the production rate data is a linear fit through the origin with a slope of 0.74 (mg/h)/(g/L).

and the droplet production rate remained constant as the precursor concentration varied. Therefore, the amount of precursor delivered was directly proportional to the precursor concentration. This translated into a production rate that was almost directly proportional to precursor concentration. Particle size also increased with increasing precursor concentration but was not directly proportional to precursor concentration and varied much less than the production rate. Figure 8 shows TEM images of nanoparticles synthesized at precursor concentrations of 10 and 100 g/L. The nanoparticles produced at lower precursor concentrations were not only smaller than those produced at higher precursor concentrations but were also more uniform in size and shape.

Considering the number concentration of particles produced in the reactor can potentially provide insights into their formation dynamics. Dividing the measured production rate by the volume corresponding to a sphere with the measured surface area mean diameter shows that the particle number concentration is rather insensitive to the precursor concentration. The estimated number concentration of particles within

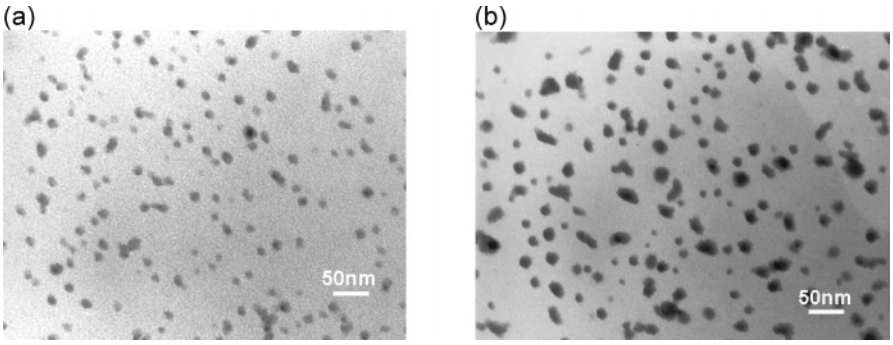

Figure 8. Precursor concentration effect on particle size and morphology. Particles shown were produced using precursor solutions containing (a) 10 g/L and (b) 100 g/L of $Te(OH)_6$ in water.

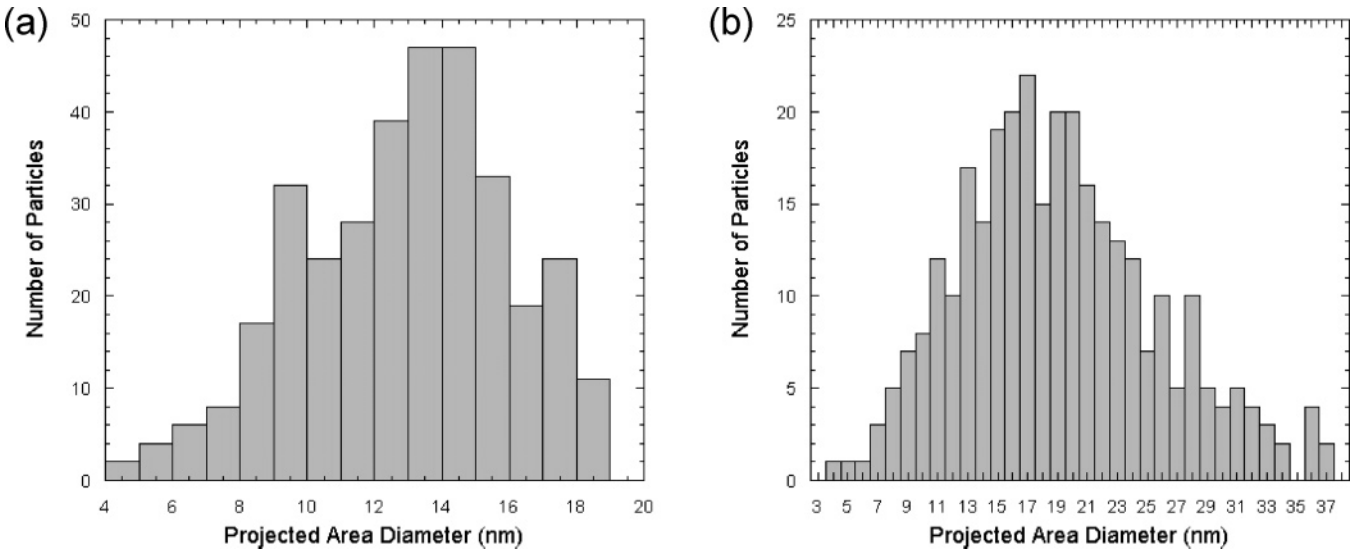

Figure 9. Precursor concentration effect on particle size distribution. Size distributions (from analysis of TEM images) for nanoparticles produced using precursor solutions containing (a) 10 g/L and (b) 100 g/L of $Te(OH)_6$ in water.

the reactor increases from about 5.6×10^8 particle/cm^3 for a precursor concentration of 10 g/L to about 1.2×10^9 particle/cm^3 for a precursor concentration of 50 g/L, but drops back to 5.8×10^8 particle/cm^3 for a precursor concentration of 100 g/L. Note that this estimate neglects particles deposited on the walls of the reactor and tubing upstream of the collection filter, and therefore, the true number concentration within the reactor is probably somewhat higher. The residence time in the reactor was roughly 0.5 s. Simple calculations of the coagulation rate of a monodisperse aerosol showed that these concentrations were near the maximum coagulation limited concentration possible after a time on the order of a second. It should also be noted that this concentration is much higher than the number concentration of solution droplets entering the reactor, which was estimated to be on the order of 10^6 droplets/cm^3. This suggests that the overall particle formation process involves complete evaporation of the precursor droplets, followed by nucleation and growth of TeO_2 particles from the vapor phase. This is confirmed by online particle size distribution measurements presented next. If the particle number concentration was completely independent of the concentration of the precursor solution, then the particle diameter would scale as the cube root of the precursor solution concentration (particle volume would be proportional to precursor solution concentration).

Size distributions of the nanoparticles synthesized at precursor concentrations of 10 and 100 g/L were obtained from TEM images like those shown in Figure 8 using the public domain image analysis software ImageJ.[41] Overlapping particles were manually deleted prior to image analysis. Between 300 and 350 particles were analyzed in each case. Results of these measurements are shown in Figure 9, where the particle diameter shown is the projected area diameter. This is defined as the diameter of the sphere that has the same projected area as the imaged nonspherical particle. For particles synthesized at a precursor concentration of 10 g/L, the number mean diameter was 13.0 nm, the geometric mean diameter was 12.6 nm, and the surface area mean diameter was 14.3 nm. The size distribution in this case was relatively narrow, with a standard deviation of 3.0 nm (23% of the mean diameter) and a geometric standard deviation of 1.30. The particles synthesized at a precursor concentration of 100 g/L were larger, with a number mean diameter of 19.1 nm, a geometric mean diameter of 17.9 nm, and a surface area mean diameter of 23.5 nm. In this case, the size distribution was broader, with a standard deviation of 6.6 nm (35% of the mean diameter) and a geometric standard deviation of 1.45. These size distributions

(41) Rasband, W. S. *ImageJ, version 1.33*; National Institutes of Health: Bethesda, MD, 2004.

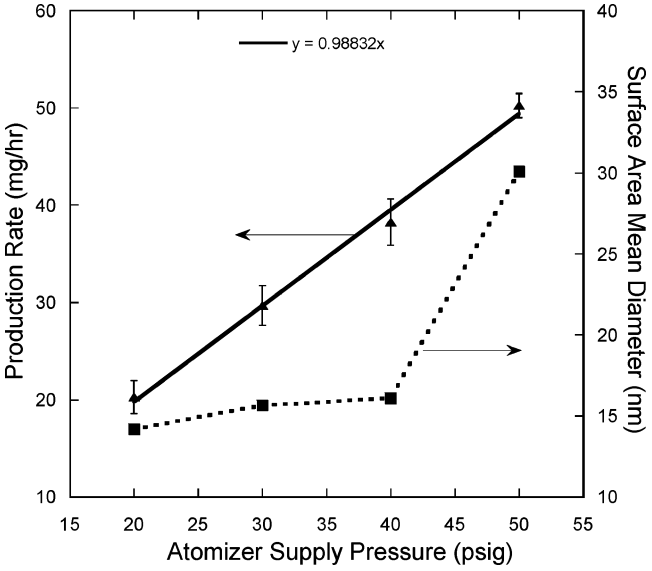

Figure 10. Effect of atomizer supply pressure on the TeO_2 nanoparticle production rate and surface area mean diameter. Error bars on the production rate are one standard deviation based on three to five replicates. The line through the production rate data is a linear fit through the origin with a slope of 0.99 (mg/h)/(psig).

are reasonably consistent with the results from BET surface area analysis, which gave surface area mean diameters of 12.6 nm for a precursor concentration of 10 g/L and 25.3 nm for a precursor concentration of 100 g/L. The increase in polydispersity with increasing precursor concentration may be explained based on the fact that a higher precursor concentration will leave larger precursor droplets (of liquid $Te(OH)_6$) after water removal, which occurs primarily in the diffusion drier. Larger $Te(OH)_6$ droplets will evaporate more slowly, resulting in a wider range of particle growth times within the reactor and a broader size distribution.[42]

Effect of Pressure Supply to Atomizer. The pressure supplied to the atomizer also affects the nanoparticle synthesis since it directly controls the gas flow rate through the atomizer. The gas flow rate through the atomizer increased linearly from about 6.5 to 12.5 slm as the supply pressure was increased from 20 to 50 psig.[43] The droplet concentration decreased somewhat with increasing supply pressure, so that the total droplet output increased more slowly than the gas flow rate.[43] Increasing the gas flow rate not only decreases the residence time in the reactor, but may also reduce the loss of droplets in the diffusion drier and plumbing leading to the reactor. In this series of experiments, we fixed all other operating parameters at the values shown in Table 1 and only varied the pressure supply to the atomizer. We measured the production rate and surface area mean diameter as functions of the atomizer supply pressure. The results are shown in Figure 10. As the pressure supply to the atomizer was increased from 20 to 50 psig, the production rate increased from 21 to 49 mg/h. When it was increased from 20 to 40 psig, the particle surface area mean diameter increased slightly from 14.2 to 16.1 nm. It then increased sharply to 30.1 nm for a supply pressure of 50 psig. The amount of precursor delivered by the atomizer increased with increasing supply pressure, but by a smaller fraction than the increase in production rate observed. According to May,[43] the delivery rate of water droplets from the atomizer used here increased from 3.3 mL/h at a supply pressure of 20 psig to 3.8 mL/h at a supply pressure of 50 psig, while the total liquid consumption rate (droplets plus water vapor) increased from 8.7 to 14 mL/h. May[43] also reported a jump in the droplet delivery rate from 3.4 mL/h at 40 psig supply pressure to 3.8 mL/h at 50 psig supply pressure, and this may contribute to the slightly sharper increase in production rate between 40 and 50 psig as compared to lower supply pressures. However, it could not explain the dramatic increase in particle diameter. The droplet delivery rate increased by about 15% between when the supply pressure was increased from 20 to 50 psig, while the total liquid consumption (droplets plus water vapor) increased by about 61% over this range. The increase in total $Te(OH)_6$ precursor delivered should lie between these two values since some of the water vapor delivered evaporated from droplets that also leave the atomizer. Most of it, however, evaporated from large droplets that were recirculated within the atomizer. Over this same range, the particle production rate increased by 119%. Thus, it seems that the most important effect of increasing the atomizer supply pressure was to reduce the loss of droplets flowing to the reactor and particles leaving the reactor by decreasing the residence time in all parts of the system so that deposition on the tube walls and within the diffusion drier was reduced.

Effect of System Pressure. We also studied the effect of the system pressure on the synthesis of telluria nanoparticles, by preparing particles at 7, 14, and 20 psia, with all the other operating parameters fixed at the values shown in Table 1. The operating pressure had minimal effect on the production rate, which was 35.5, 38.3, and 37.5 mg/h, at 7, 14, and 20 psia, respectively. However, the operating pressure did have an effect on the surface area mean diameter, which was 15.1, 16.1, and 20.4 nm at 7, 14, and 20 psia, respectively. The primary effect of increased operating pressure is to increase the precursor and particle concentrations and to increase the residence time in the system. The coagulation rate for small particles is insensitive to pressure but increases with concentration. So, the increase in concentration and residence time leads to increased coagulation and formation of larger particles. It appears that particle losses to the walls of the reactor system are insensitive to pressure. For diffusional loss of small particles, the increased residence time is offset by a decrease in the particle diffusion coefficient with increasing pressure. Particle losses by impaction should decrease with increasing pressure, due to the decrease in flow velocity at higher pressure. The aerosol delivery rate may be increased at lower operating pressure (higher pressure drop across the atomizer), and this may offset any increase in losses by impaction at lower pressure.

Effect of Air Flow Rate. A small flow of air was added to the reactor to ensure that excess oxygen was present so that fully oxidized TeO_2 would be produced. We investigated the effect of changing the flow rate of air by replacing part of this flow with nitrogen. One experiment corresponded to the conditions listed in Table 1, while in the other experiment,

(42) Heine, M. C.; Pratsinis, S. E. *Ind. Eng. Chem. Res.* **2005**, *44*, 6222.
(43) May, K. R. *J. Aerosol Sci.* **1973**, *4*, 235.

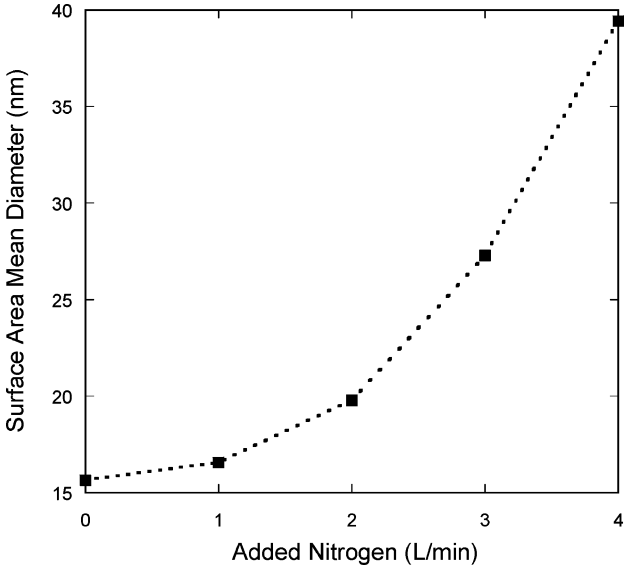

Figure 11. Effect of added nitrogen (increased total flow rate) on particle diameter.

the air flow rate was reduced from 2.0 to 0.5 L/min, and the added nitrogen flow rate was set at 1.5 L/min so that the total gas flow rate through the reactor was unchanged. The production rates in these two experiments were 38.3 and 37.0 mg/h, identical to within experimental uncertainty. The surface area mean diameters were 16.0 and 16.1 nm, also unchanged. Provided that sufficient oxygen was present to produce TeO_2, varying the nitrogen to oxygen ratio in the reactor did not have a significant effect on the production rate or size.

Effect of Total Flow Rate (Added Nitrogen). The residence time in the reactor was varied by adjusting the bypass nitrogen flow rate to change the total gas flow rate through the reactor while keeping the pressure supplied to the atomizer constant. The results show that residence time has an important and unexpected effect on the size of the nanoparticles. In this set of experiments, the pressure supplied to the atomizer was fixed at 30 psig, and other parameters were those listed in Table 1, except for the bypass nitrogen flow rate. The bypass nitrogen flow rate was increased from 0 to 4 L/min. The production rate changed very little with increased nitrogen flow. It was 29.7, 30.4, 30.8, 31.2, and 31.5 mg/h for added nitrogen flows of 0, 1, 2, 3, and 4 L/min. The influence of added nitrogen flow on the particle size was much more significant. The surface area mean diameters based on the BET surface area measurements were 15.6, 16.3, 20.1, 27.3, and 39.4 nm for added nitrogen flows of 0, 1, 2, 3, and 4 L/min, as shown in Figure 11. The slight increase of the production rate can probably be attributed to a decrease in the loss of nanoparticles by diffusion to the walls of the reactor and downstream tubing at shorter residence times. Losses of precursor droplets in the diffusion drier should be unchanged since the extra nitrogen was added downstream of it.

The sharp increase in the particle diameter was unexpected and is more difficult to explain. The addition of nitrogen decreased the residence time in the reactor and also decreased the vapor-phase concentration of precursor molecules and particles in the reactor. These effects were also achieved by decreasing the pressure in the reactor, which did not have a dramatic effect on particle size. Both of these factors, shorter residence time and lower concentrations, would be expected to lead to a decrease in the particle diameter if the particles were grown by the addition of vapor-phase precursor molecules and/or particle−particle coagulation. Further investigation showed that the sharp increase in particle size at shorter residence time could be attributed to the presence of a very small number of large particles in the product due to the incomplete evaporation of the precursor droplets at shorter residence time. When such a bimodal size distribution is present, the BET surface area measurement is dominated by the small number of anomalously large particles.[27] As shown in Figure 12, more extensive TEM imaging revealed an occasional particle that was dramatically larger than the majority of the particles.

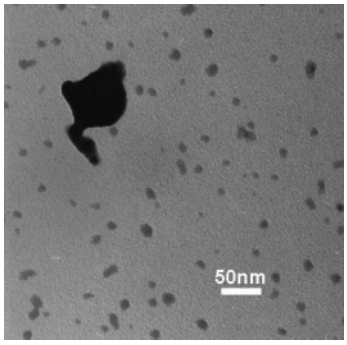

Figure 12. TEM image showing the presence of a large particle formed via incomplete evaporation at high flow rate through the reactor.

This evidence of incomplete droplet evaporation prompted us to carry out a more detailed study of the precursor droplet evaporation dynamics, using a scanning mobility particle spectrometer (SMPS) for online size distribution measurements as described in the Experimental Procedures. The particle size distributions resulting from different reaction conditions provide substantial insight into the particle formation process. Figure 13 shows the size distributions of nanoparticles produced at constant reaction conditions except for the furnace temperature, with a precursor concentration of 10 g/L (a and b) or 100 g/L (c and d). The furnace temperature was increased from room temperature to 400, 600, 650, 660, 680, 700, and 800 °C. Panels a and c of Figure 13 show this data on a linear concentration scale, while panels b and d show the same data on a logarithmic concentration scale. When the furnace was at room temperature and the precursor concentration was 10 g/L, the particles had a geometric mean diameter of 88 nm. This size distribution should be essentially the same as that of the droplets entering the reactor. This is much smaller than the average droplet size produced by the nebulizer, because before entering the reactor the droplets pass through a mist collector that removes large droplets by impaction, then a diffusion drier that removes most of the water. The size distribution at a furnace temperature of 400 °C is similar to the one at room temperature, with a slightly smaller geometric mean diameter of 68 nm. When the furnace temperature was further increased to 600 °C, a second mode appeared in the aerosol size distribution, peaking at around 13 nm. This is attributed to homogeneous nucleation of new

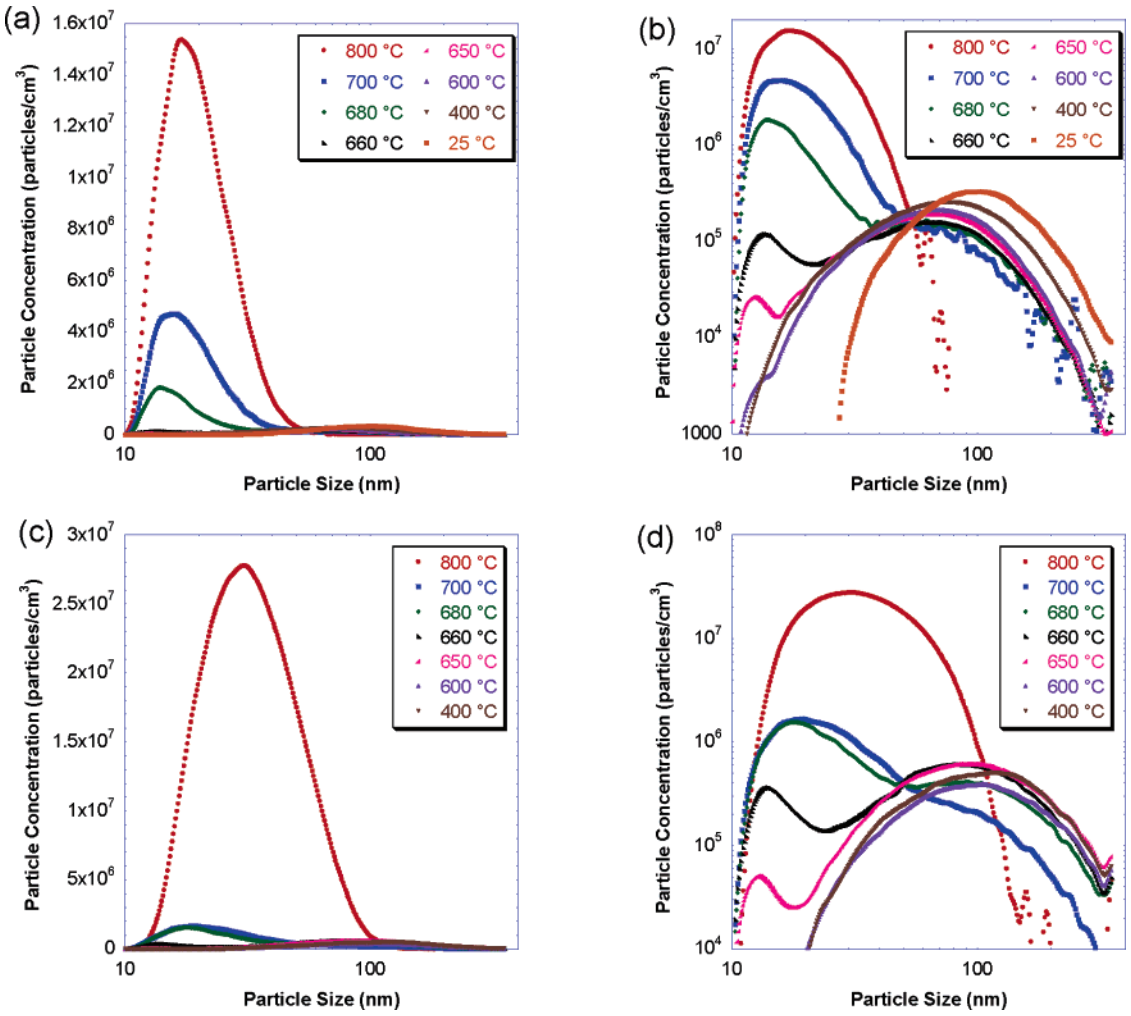

Figure 13. Particle size distributions measured by SMPS at different furnace temperatures for (a and b) 10 g/L precursor concentration and (c and d) 100 g/L precursor concentration. Panels a and c show concentration on a linear scale, while panels b and d use a log scale to make the onset of homogeneous nucleation of small particles between 600 and 700 °C visible.

particles from material that has evaporated from the larger droplets. The size distribution was still dominated by the large particles that consisted of unreacted telluric acid, consistent with the XPS spectrum of particles formed at 600 °C, which was dominated by telluric acid. Upon further increasing the reaction temperature to 650, 660, 680, and 700 °C, the small diameter mode of the size distribution increased dramatically in particle concentration, and slightly in particle size, as the large diameter peak shrunk in both size and concentration. This can be attributed to increased evaporation of the large particles and increased homogeneous nucleation of small particles. The size increase of the small particles may result from increased agglomeration with increasing particle concentration as well as from faster particle growth at higher temperature and vapor-phase concentrations. For a reactor temperature of 700 °C, the large particle peak was almost gone, and for the reaction temperature of 800 °C, it was completely gone. The concentration of the smaller nanoparticles continued to increase. Thus, at 800 °C, the precursor particles evaporated fully, and only the much smaller, homogeneously nucleated TeO_2 nanoparticles were present. For a precursor concentration of 100 g/L, the results were qualitatively the same as for 10 g/L but with a larger particle diameter for both modes of the size distribution.

Figure 14 shows the particle concentration, geometric mean diameter, and geometric standard deviation of the particles as the temperature was increased. The total particle concentration remained almost constant for temperatures up to 650 °C, then sharply increased with an increasing temperature from 660 to 800 °C. The total nanoparticle concentration increased by about a factor of 40 and a factor of 55, for precursor concentrations of 10 and 100 g/L as the temperature increased from 600 to 800 °C. For temperatures up to 650 °C, the geometric mean diameter decreased slightly with increasing temperature, then decreased sharply between 650 and 700 °C, as the size distribution went from being dominated by the large unevaporated precursor particles to being dominated by the small homogeneously nucleated particles. The geometric mean diameter increased slightly between 700 and 800 °C. This can be attributed to increased particle agglomeration at higher particle concentrations as well as more rapid particle growth at higher precursor concentrations in the vapor phase. Figure 14c shows that the geometric standard deviation of the size distribution goes through a maximum near 660 °C, where the size

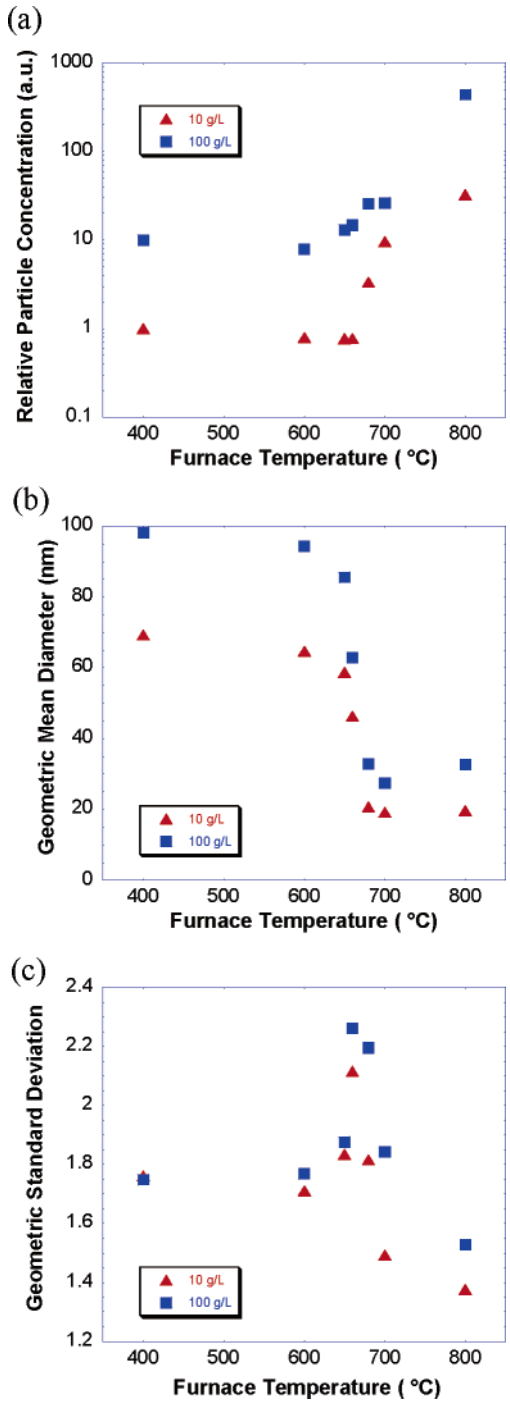

Figure 14. Characteristics of the particle size distribution as a function of reactor temperature. (a) Total particle concentration, arbitrarily scaled to concentrations of 1 and 10 at 400 °C, (b) geometric mean diameter, and (c) geometric standard deviation.

distribution is bimodal with comparable peak concentrations in both modes. At 800 °C, it approaches the value of 1.4 that is typical of coagulation limited particle growth. The geometric standard deviation for the 100 g/L precursor concentration is consistently higher than that for the 10 g/L precursor concentration. This is consistent with the size distributions obtained from TEM imaging, as described previously.

Figure 15 shows the influence of total gas flow rate through the reactor (residence time) on the particle size distribution for an atomizer supply pressure of 30 psig. When

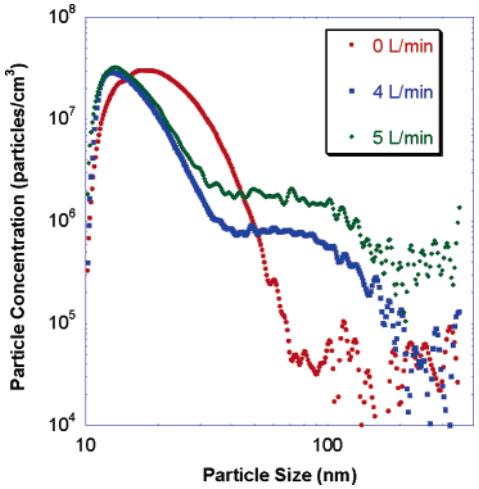

Figure 15. Effect of increased gas flow rate (reduced residence time) on particle size distribution for a reactor temperature of 800 °C and precursor concentration of 10 g/L. Note that the dilution ratio is not necessarily the same for the three size distributions.

4 L/min of nitrogen was added to the flow entering the reactor, the total flow through the reactor was increased by about 45%, and therefore, the residence time in the reactor was decreased by about 30%. As discussed previously, we were surprised to find that the average diameter based on the BET surface area measurement increased when the residence time was decreased in this manner. The results in Figure 15 help to clarify this. Upon increasing the bypass nitrogen flow rate from 0 to 4 L/min, the particle size distribution shifted to a smaller diameter. Further increasing this flow to 5 L/min resulted in an additional slight decrease in the peak particle size. However, as shown in Figure 15, where the particle concentration is presented on a logarithmic scale, at these higher flow rates (shorter residence times), a small second mode appears in the size distribution, in the diameter range of 60−100 nm. This can be attributed to incomplete evaporation of a relatively small number of precursor droplets. This is consistent with the presence of a few large particles as observed in the TEM image shown in Figure 12. Because the surface area mean diameter measured by BET is very heavily weighted toward larger particles, this relatively small number of large particles has a dramatic effect. Surface area measurement is not an effective means of characterizing the diameter of particles with a bimodal size distribution.[27]

Semiquantitative simulations of the flow and heat transfer in the reactor showed that this incomplete evaporation results from incomplete heating of the carrier gas when the gas flow rate was increased above about 10 slm. Panels a and b of Figure 16 show temperature profiles for conditions that approximate the reactor used here. Since we do not know the details of the wall temperature profile, these are not expected to be quantitatively correct. Nonetheless, they should accurately capture the overall features of heating in our reactor system. Simulations were carried out using the CRESLAF code[44] for reacting boundary layer flow in a tube. We modeled a pure nitrogen flow with no chemical reactions occurring in the gas phase or on the tube walls. In our experiments, the precursor droplets constituted less than 0.1% of the mass flow through the reactor and therefore have little

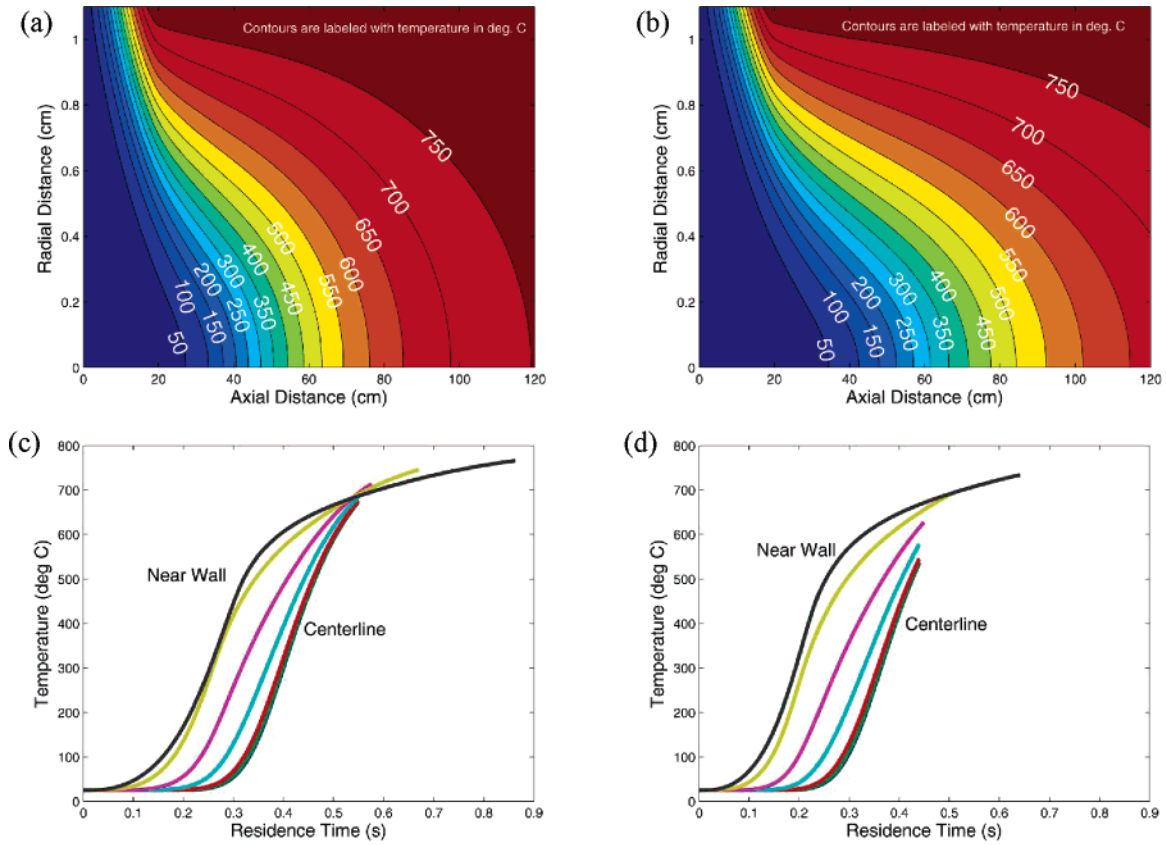

Figure 16. Simulated temperature profiles in a tube with an inner radius of 1.1 cm (0.87 in. diameter) and a wall temperature increasing linearly from 25 to 800 °C over the first 20 cm of its length, then fixed at 800 °C for the remainder of its length. Nitrogen at 1 atm and 25 °C enters the tube in plug flow at a velocity of 50 cm/s (a and c) or 70 cm/s (b and d). These correspond to total flow rates of 10.4 and 14.6 slm, respectively. Panels a and b show isotherms within the reactor. Panels c and d show the temperature vs residence time along various streamlines, ranging from the center line of the tube to a near-wall streamline that starts 1.1 mm from the wall (~90% of the tube radius, enclosing ~81% of the flow). The curves end at an axial position of 90 cm.

effect on the heat capacity. For much higher droplet loadings, as would be obtained by using an ultrasonic atomizer to achieve higher reactor throughput, the heat capacity and heat of vaporization of precursor droplets would have to be considered. The end of the heated region of our reactor system was at an axial distance of about 90 cm (70 cm past the end of the increasing temperature ramp). As can be seen from the profiles in Figure 16, the center line temperature at this point dropped by more than 100 °C (from >650 °C to <550 °C) when the flow through the reactor was increased by 40%.

Panels c and d present temperature profiles versus residence time along various streamlines in the reactor. This shows that the heating rate was quite similar along different streamlines and for different flow rates. However, the onset of heating was shifted downstream for streamlines near the center of the reactor and at higher flow rates. Thus, the center line temperature did not reach the wall temperature under our typical operating conditions. These heat transfer limitations could readily be reduced by splitting the flow among several smaller tubes. Heat transfer to droplets from the surrounding gas was substantially faster than the heat transfer from the reactor walls to the flowing gas. A characteristic time for particle heating is given by R^2/α, where α is the thermal diffusivity of the particle and R is the particle radius.[45] Thermal diffusivities of liquids are on the order of 10^{-5} cm^2/s, which gives characteristic heat transfer times ranging from 250 μs for 1 μm diameter droplets to 25 ns for 10 nm diameter droplets. Thus, in our reactor system, the rate limiting step in droplet heating and evaporation will be heat transfer from the reactor wall to the carrier gas.

The precursor evaporation in the reactor, as evidenced from the change in size distributions shown previously, contrasts sharply with measurements of precursor evaporation made using thermogravimetric analysis (TGA). TGA was performed on both telluric acid powder and solutions in water. Figure 17a shows the TGA results for telluric acid powder heated at a rate of 5.0 °C/min, which is much slower than the heating rate in the reactor. The sample begins to lose weight at about 140 °C, which is just above the melting point of telluric acid (136 °C). At about 600 °C, the curve reached a plateau, with about 69 wt % remaining. This is simply the ratio of the molecular weights of TeO_2 and $Te(OH)_6$ (160:230), suggesting that at this heating rate, the liquid telluric acid was fully converted to solid TeO_2 well below 600 °C, with negligible evaporation. Finally, the mass dropped sharply at about 860 °C. This is attributed to the decomposition of TeO_2, which is consistent with the obser-

(44) Coltrin, M. E.; Moffat, H. K.; Kee, R. J.; Rupley, F. M. *CRESLAF: A Fortran Program for Modeling Laminar, Chemically Reacting, Boundary-Layer Flow in Cylindrical or Planar Channels*, Report No. SAND93-0478; Sandia National Laboratories: Albuquerque, NM, 1993.

(45) Bird, R. B.; Stewart, W. E.; Lightfoot, E. N. *Transport Phenomena*, 2nd ed.; John Wiley and Sons: New York, 2002.

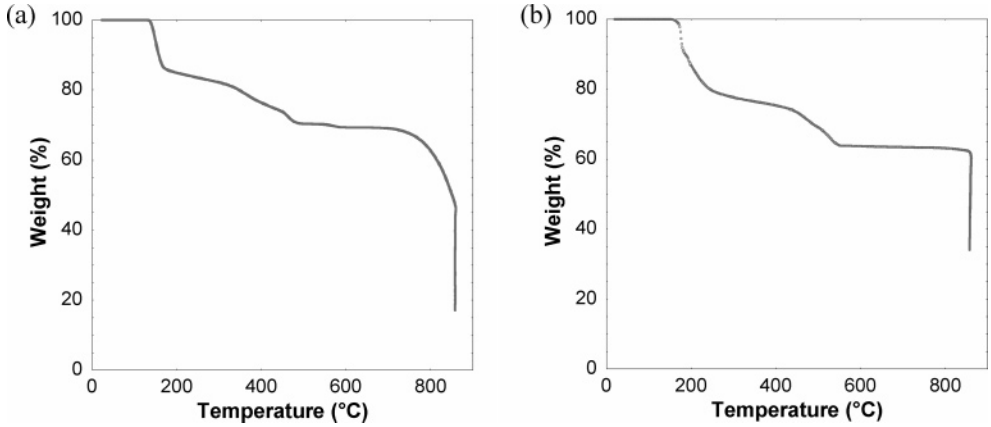

Figure 17. Results of thermogravimetric analysis of telluric acid heated at (a) 5 °C/min and (b) 100 °C/min.

vation of metallic tellurium in some of our nanoparticle samples produced at 1000 °C.

Similar TGA results were obtained staring from a solution of 50 g/L of telluric acid in water, with 95% mass loss near 100 °C followed by the same profile observed for pure telluric acid above 125 °C. As shown in Figure 17b, a similar profile was observed for pure telluric acid at a higher heating rate of 100 °C/min, which is still much slower than in the reactor, where the heating rate is on the order of 50 000 °C/min. At a heating rate of 100 °C/min, the constant mass plateau was at about 64% of the original mass, suggesting that a small amount of evaporation may have occurred. These results show that there is a competition between evaporation of $Te(OH)_6$ and its reaction to form TeO_2. At heating rates attainable in thermogravimetric analysis, the reaction to form TeO_2 dominates, but at the much higher heating rates experienced by droplets in the spray pyrolysis reactor, complete evaporation occurs. Differences in mass transport in the two systems (bulk sample vs small aerosolized particles) may also be important. This clearly shows that the spray pyrolysis approach provides a unique means of delivering precursor vapor in this system. One could not use the alternative approach of heating liquid telluric acid in a bubbler and delivering it as a vapor since it would convert to solid TeO_2 in the bubbler before evaporating significantly.

Conclusion

Synthesis of tellurium dioxide nanoparticles in the vapor phase using spray pyrolysis with an inexpensive and environmentally friendly precursor (telluric acid in water) has been demonstrated. The resulting nanoparticles were amorphous with mean primary particle diameters ranging from 10 to 40 nm. Nitrogen physisorption (the BET method), X-ray diffraction (XRD), transmission electron microscopy (TEM) imaging, selected area electron diffraction, and X-ray photoelectron spectroscopy (XPS or ESCA) analysis were employed to characterize the as-synthesized nanoparticles and crystallized particles. A furnace temperature of 800 °C was identified as optimal for producing stoichiometric amorphous TeO_2. When the precursor concentration and pressure supply to the atomizer were increased, both particle production rate and average particle size increased. Increasing the flow velocity through the reactor had minimal effect on the production rate but surprisingly led to a dramatic increase in the particle diameter. This can be attributed to incomplete evaporation of a small fraction of precursor particles. Detailed online measurements of aerosol particle size distributions leaving the reactor showed that reactor wall temperatures above 700 °C were required for complete evaporation of the precursor droplets. The droplet evaporation dynamics in the reactor were shown to be much different than for bulk telluric acid heated at slower rates. At slower heating rates, $Te(OH)_6$ converted to TeO_2 without evaporating, but at the high heating rates attained in the spray pyrolysis reactor, it evaporated fully, and TeO_2 particles nucleated homogeneously from the vapor phase, allowing production of small particles. Spray pyrolysis is a promising method for environmentally friendly synthesis of TeO_2 nanoparticles with sizes small enough to make them essentially non-scattering for visible light. This should be useful in linear and nonlinear refractive index engineering of nanocomposites and other applications.

Acknowledgment. We thank Prof. James M. O'Reilly and Dr. Jia Liu for many useful discussions. We thank Dr. Y. Hu and Prof. Eli Ruckenstein for help with the BET measurements and use of their equipment. This work was partially supported by a grant from the University at Buffalo (SUNY) Office of the Vice President for Research.

CM062257N